ACS OMEGA

Article

Cite This: ACS Omega 2018, 3, 13227−13238

http://pubs.acs.org/journal/acsodf

One-Step Synthesis, Structure, and Band Gap Properties of SnO_2 Nanoparticles Made by a Low Temperature Nonaqueous Sol−Gel Technique

Mohamed Karmaoui,*[†,‡] Ana Belen Jorge,[§] Paul F. McMillan,[∥] Abil E. Aliev,[∥] Robert C. Pullar,[†] João António Labrincha,[†] and David Maria Tobaldi*[†]

[†]Department of Materials and Ceramic Engineering/CICECO—Aveiro Institute of Materials, University of Aveiro, Campus Universitário de Santiago, 3810-193 Aveiro, Portugal

[‡]Département de Génie Chimique, Faculté de Chimie, Université des Sciences et de la technologie Mohamed-Boudiaf El Mnaouar, BP 1505, Bir El Djir, 31000 Oran, Algeria

[§]Materials Research Institute, School of Engineering and Materials Science, Queen Mary University of London, Mile End Road, E1 4NS London, U.K.

[∥]University College London, Christopher Ingold Building, 20 Gordon Street, WC1H 0AJ London, U.K.

Supporting Information

ABSTRACT: Because of its electrically conducting properties combined with excellent thermal stability and transparency throughout the visible spectrum, tin oxide (SnO_2) is extremely attractive as a transparent conducting material for applications in low-emission window coatings and solar cells, as well as in lithium-ion batteries and gas sensors. It is also an important catalyst and catalyst support for oxidation reactions. Here, we describe a novel nonaqueous sol−gel synthesis approach to produce tin oxide nanoparticles (NPs) with a low NP size dispersion. The success of this method lies in the nonhydrolytic pathway that involves the reaction between tin chloride and an oxygen donor, 1-hexanol, without the need for a surfactant or subsequent thermal treatment. This one-pot procedure is carried out at relatively low temperatures in the 160−260 °C range, compatible with coating processes on flexible plastic supports. The NP size distribution, shape, and dislocation density were studied by powder X-ray powder diffraction analyzed using the method of whole powder pattern modeling, as well as high-resolution transmission electron microscopy. The SnO_2 NPs were determined to have particle sizes between 3.4 and 7.7 nm. The reaction products were characterized using liquid-state ^{13}C and ^{1}H nuclear magnetic resonance (NMR) that confirmed the formation of dihexyl ether and 1-chlorohexane. The NPs were studied by a combination of ^{13}C, ^{1}H, and ^{119}Sn solid-state NMR as well as Fourier transform infrared (FTIR) and Raman spectroscopy. The ^{13}C SSNMR, FTIR, and Raman data showed the presence of organic species derived from the 1-hexanol reactant remaining within the samples. The optical absorption, studied using UV−visible spectroscopy, indicated that the band gap (E_g) shifted systematically to lower energy with decreasing NP sizes. This unusual result could be due to mechanical strains present within the smallest NPs perhaps associated with the organic ligands decorating the NP surface. As the size increased, we observed a correlation with an increased density of screw dislocations present within the NPs that could indicate relaxation of the stress. We suggest that this could provide a useful method for band gap control within SnO_2 NPs in the absence of chemical dopants.

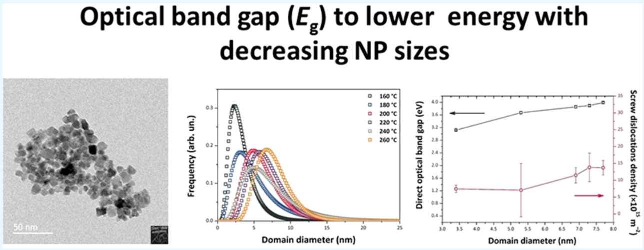

1. INTRODUCTION

As one of the most important members of the transparent conducting oxide (TCO) class of materials, the electronic and optical properties of pure and doped SnO_2 have been investigated extensively.[1,2] Tin oxide (SnO_2) nanoparticles (NPs) are being developed for applications ranging from their incorporation as an opacifier in ceramic glazes to advanced technologies including gas sensors, lithium-ion batteries, low emission window coatings, touch screens, sensitized solar cells, field emission flat displays, and other optoelectronic devices.[3] For each of these applications, it is important to have a simple, low cost and scalable synthesis approach that will produce NPs within a narrow distribution of particle sizes.[2] Various synthesis strategies have been developed to produce SnO_2 NPs with different size ranges and distributions.[4−11] These processes usually require use of high temperatures, high boiling point or mixed solvents, and expensive organic tin precursors that are often toxic and require a complicated synthesis procedure. The

Received: August 21, 2018
Accepted: October 1, 2018
Published: October 15, 2018

ACS Publications

DOI: 10.1021/acsomega.8b02122

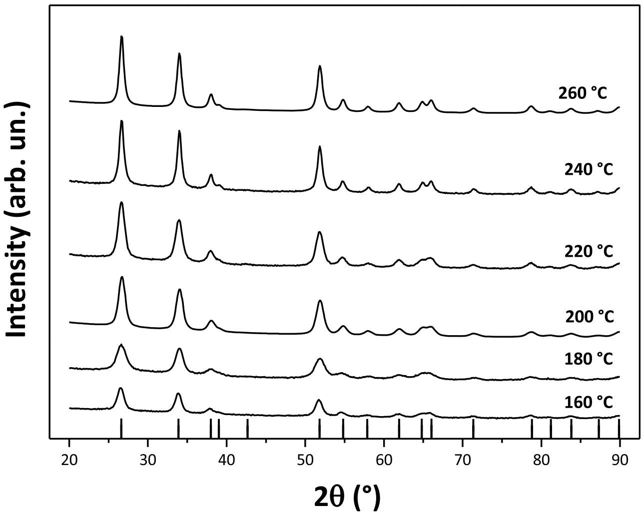

Figure 1. Powder X-ray diffraction patterns (Cu Kα radiation) of the SnO_2 specimens prepared at different temperatures. The vertical lines below indicate the expected reflections for the rutile structured cassiterite phase.

experimental parameters required for such reactions run counter to the ability to produce highly crystalline nanosized structures with controllable properties. To avoid the problems associated with several of the proposed routes, synthetic routes that avoid the use of water and toxic solvents or surfactants and/or toxic solvents have been investigated.[12,13] It is now important to develop one-pot synthesis methods that can produce crystalline SnO_2 NPs with tuneable particle sizes and band gap properties. Nonaqueous sol−gel processing is a flexible and powerful approach to obtain functionally active NPs.[14−18] Here, we present a facile, one-pot, nonhydrolytic synthesis of SnO_2 NPs with controllable average size and with a narrow size distribution at low temperature.

Bulk crystalline SnO_2 with a tetragonal rutile structure (cassiterite phase) is an n-type direct gap semiconductor with the band gap (E_g) equal to 3.6 eV (344 nm). It provides an archetypal TCO, having up to 97% transparency across the visible spectrum.[19] This large value is comparable with that required for complete transparency throughout the visible range (i.e., E_g > 3.1 eV). A large amount of research has been devoted to modifying the SnO_2 conduction band minimum and consequently modifying its optical absorption properties. These can be tuned by substituting elements such as such as F, Sb, or Pb on the anion or cation sites, by controlling NP size and morphology,[1,2] or by causing internal strain within materials prepared as thin-film samples.[20] Nearly all of the studies to date have reported that E_g typically increases for smaller NP sizes.[21−26]

The nonaqueous sol−gel process is based on the reaction between tin(IV) tetrachloride $Sn(Cl)_4$ and 1-hexanol, leading to the formation of SnO_2 NPs with a narrow dispersion and average sizes between 3.4 and 7.7 nm by varying the synthesis temperature between 160 and 260 °C. Both reagents are readily available, and the potentially scalable process yields NP materials that can be used without further processing. Unusually, we observed that E_g for our materials increased as the NPs became larger, with values determined to lie between 2.22 (indirect) and 3.12 (direct) eV for 3.4 nm NP sizes, to 3.53−3.99 eV for 7.7 nm particles. In order to investigate the origin of these unusual electronic structure changes, we carried out detailed structural and spectroscopic investigations of our SnO_2 NPs using a combination of X-ray powder diffraction (XRPD), high-resolution transmission electron microscopy (HRTEM), UV−visible, IR and Raman, and ^{119}Sn, ^{13}C, and ^{1}H nuclear magnetic resonance (NMR) spectroscopy techniques. Analysis of the XRPD data using the whole powder pattern modeling (WPPM) technique[27−33] revealed the presence of axial strains and screw dislocations within the NPs. These strains are correlated with the presence of organic ligands detected by NMR, IR, and Raman spectroscopy and likely determine the unexpected band gap behavior, as well as providing possibilities for further modification and functionalization of the NP surfaces.

2. RESULTS AND DISCUSSION

2.1. X-ray Diffraction and HRTEM. The SnO_2 NPs crystallized with the rutile structure (space group $P4_2/mnm$), with no additional impurity phases detected by X-ray examination (Figure 1). Initial examination of the XRPD patterns indicates that the peaks became sharper and better resolved with increasing NP size at higher synthesis temperature. We then applied WPPM analysis to the observed XRPD profiles.[27,34] This approach provides information on the average crystalline domain size of the SnO_2 NPs and edge and screw dislocation densities (Table 1 and Figure 2); it has also been applied recently to solve both size and defect concentration in the SnO_2 system.[33,35,36] The almost flat nature of the residual line, displayed in Figure 2, indicates an excellent agreement between the experimental data and the model; this also suggests that the assumption of spherical shape for the investigated SnO_2 nanodomains is likely appropriate. The log-normal size distributions of the SnO_2 NPs synthesized at different temperatures shown in Figure 3 agree generally with the particle size distributions obtained from the HRTEM images described below. However, we note that the X-ray diffraction data and modeling provide more statistically representative sampling for the overall specimens than analysis of the TEM images. The unit cell volumes did not vary significantly as a function of synthesis temperature, but small changes in the tetragonal distortion of the SnO_2 unit cell were observed, primarily that the c/a ratio increased slightly with the increasing synthesis temperature (Table 1). The average crystalline domain diameter of SnO_2 at 160 °C found by WPPM analysis was 3.4 nm with a tail in the log-normal size distribution function extending to ∼10 nm (Table 1, Figure 3). Increasing the synthesis temperature led to a gradual increase in the average crystalline domain diameter—this became 6.9 nm at 220 °C and 7.7 nm by 260 °C. As shown in Table 1 and Figure 3, all the probability distributions have a positive skewness, with some dispersion around the tails to larger NP sizes. The number of screw dislocations "ρ_e" was determined to be greater than that of edge dislocations in all of the samples investigated (Table 1). The number of the edge dislocations did not change, whereas the density of screw dislocations "ρ_s" increased slightly as a function of the synthesis temperature.[33] The population of screw dislocations also exhibited a wider distribution about the mean for syntheses carried out at 180 °C (Figure 4).

The effects of synthesis temperature on the size, morphology, and development of defects within the SnO_2 NPs were further investigated using HRTEM (Figure 5 and Table 2). All of the NPs exhibited a high degree of crystallinity, with lattice fringes matching the cell parameters of rutile-

Table 1. Results of WPPM Modeling and Refinement from the X-ray Powder Diffraction Data, Including Unit Cell Parameters, Tetragonality (c/a), Crystalline Domain Diameters (Average, Mode, and Skewness of the log-Normal Size Distribution), and Dislocation Densities (Edge and Screw, ρ_e and ρ_s, Respectively) of Synthesized SnO_2 NPs

	agreement factors			unit cell parameters (nm)				crystalline domain diameter (nm)			dislocation density ($\times 10^{15}$ m^{-2})	
synthesis temperature (°C)	R_{wp} (%)	R_{exp} (%)	χ^2	$a = b$ (nm)	c (nm)	volume (nm^3)	c/a	average	mode	skewness	ρ_e	ρ_s
160	2.25	1.38	1.64	0.4751(1)	0.3185(1)	0.072(1)	0.6703	3.4(1)	2.3(1)	1.7(1)	1.0(7)	1.3(1)
180	1.85	1.34	1.38	0.4749(1)	0.3186(1)	0.072(1)	0.6709	5.3(2)	3.1(1)	2.2(1)	1.0(5)	1.2(8)
200	2.20	1.68	1.31	0.4750(1)	0.3189(1)	0.072(1)	0.6713	6.2(4)	4.9(3)	1.3(1)	1.0(7)	1.4(1)
220	1.94	1.33	1.46	0.4748(1)	0.3190(1)	0.072(1)	0.6719	6.9(2)	5.7(2)	1.1(1)	1.0(1)	1.7(2)
240	2.03	1.34	1.51	0.4748(1)	0.3188(1)	0.072(1)	0.6714	7.2(3)	5.0(2)	1.7(1)	1.0(3)	1.9(5)
260	2.04	1.31	1.56	0.4749(1)	0.3189(1)	0.072(2)	0.6714	7.7(1)	6.7(1)	0.9(1)	1.0(5)	1.9(2)

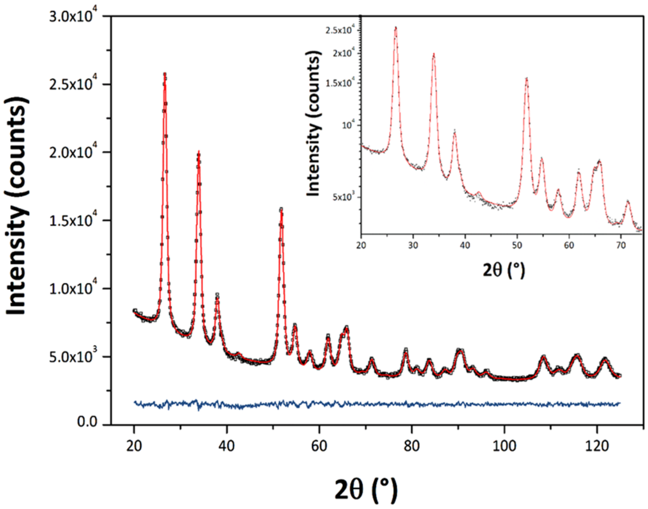

Figure 2. Typical output of the WPPM modeling protocol applied to the observed X-ray diffraction pattern of a specimen synthesized at 220 °C. The black open squares represent the observed data, and the red continuous line represents the refined fit. The blue continuous line below shows the difference between observed and calculated profile. The log-scale plot (up to 75° 2θ) shown in the inset highlights details in the peak tail and background region.

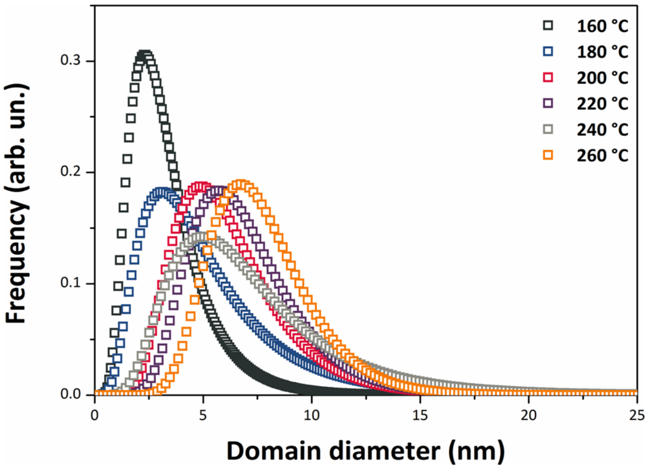

Figure 3. SnO_2 NP size distributions obtained from WPPM modeling.

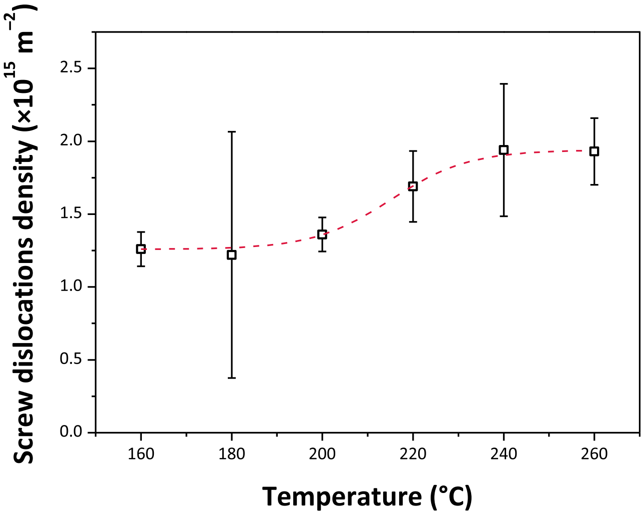

Figure 4. Evolution of screw dislocation densities with the synthesis temperature. The red dashed line represents a sigmoidal fit obtained using a sigmoidal Boltzmann function (R^2 = 0.997).

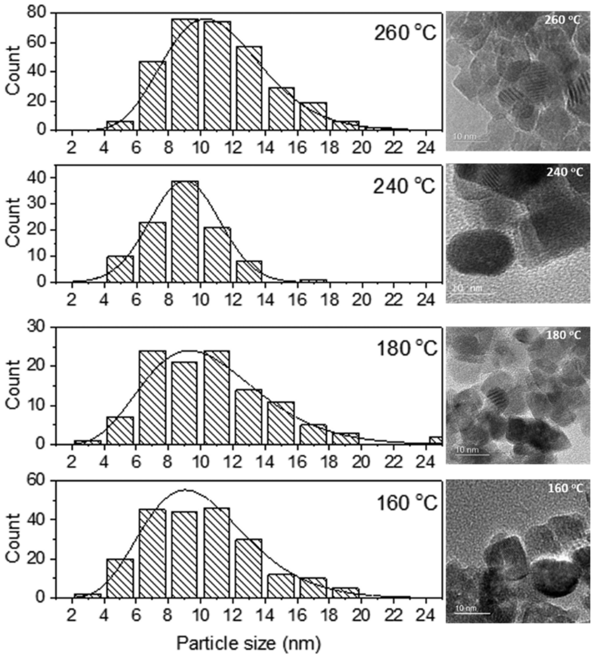

Figure 5. Particle size distribution (left) of SnO_2 NPs prepared at 160, 180, 240, and 260 °C from the analysis of HRTEM images (right).

structured SnO_2 (Figure 6). Our HRTEM images provided direct evidence for the existence of screw as well as edge dislocations within the SnO_2 NP samples deduced from the WPPM XRPD analysis (Figure 6). The SnO_2 crystallite sizes

DOI: 10.1021/acsomega.8b02122
ACS Omega 2018, 3, 13227−13238

Table 2. HRTEM Particle Size Distributions Obtained by Analysis of Images for Samples Prepared at 160, 180, 240, and 260 °C

temperature (°C)	average size (nm)	minimum size (nm)	maximum size (nm)	standard deviation
160	10.2	4.0	19.5	3.4
180	10.6	4.0	24.7	3.9
240	9.0	4.50	17.3	2.2
260	11.2	4.7	21.2	3.1

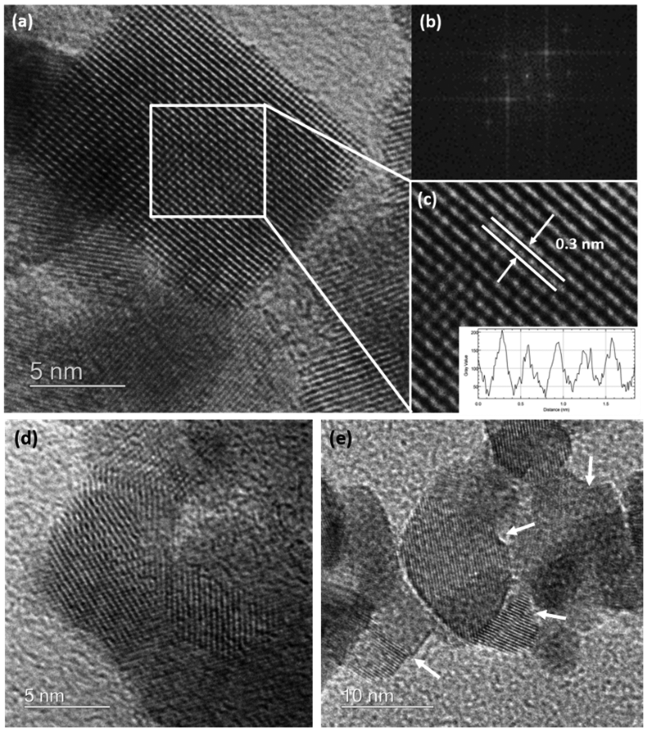

Figure 6. (a) HRTEM image of a SnO_2 sample prepared at 180 °C along with (b) its Fourier transform; (c) detail of the image showing lattice fringes with spacing ~0.3 nm corresponding to the *c* axis dimension of rutile structured SnO_2. Inset: Atomic density plot profile highlighting the spacing between lattice fringes; (d,e) HRTEM images showing the presence of screw and edge dislocations within NPs from this sample.

estimated from the recorded images ranged between 2 and 11 nm, generally consistent with our WPPM analysis of the XRPD data, although that analysis provides a more complete average over the entire sample.

2.2. Liquid Phase NMR Spectroscopy. In order to study the reaction of 1-hexanol with $SnCl_4$ during the synthesis, the supernatant liquid was filtered to remove the SnO_2 solid precipitate, and analyzed using liquid ^{1}H and ^{13}C NMR spectroscopy. The ^{13}C NMR spectrum is shown in Figure 7 (the ^{1}H NMR spectrum is included in the Supporting Information file, Figure S1). From the analysis of this spectrum, the presence of 1-hexanol (with the C1 carbon at 62.8 ppm), dihexyl ether (with the C1 carbon at 71.1 ppm), and 1-chlorohexane (with the C1 carbon at 45.1 ppm) was determined (Table S1). All other peaks from these three hydrocarbons corresponding to hexane carbons C2−C6 appear in the same region at 14−33 ppm. The formation of the dihexyl ether component was deduced from the analysis of the solid-state ^{13}C MAS NMR spectra, described in the following section.

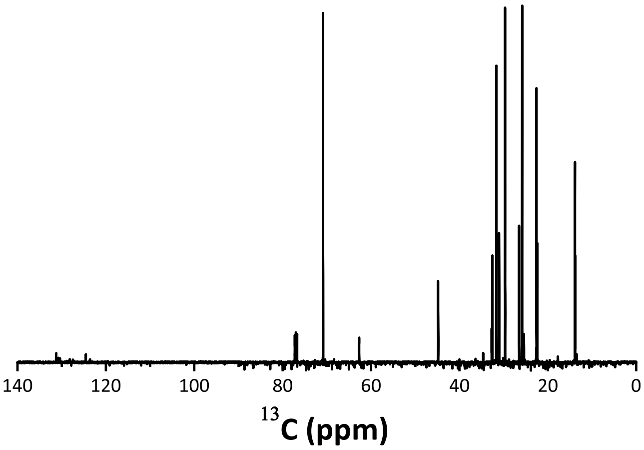

Figure 7. ^{13}C NMR spectrum of the reaction solution after removal of the NPs.

2.3. Solid-State NMR of SnO_2 NPs. The ^{13}C MAS NMR spectra of our samples are consistent with the production of 1-hexanol ($C_6H_{13}OH$), and also dihexyl ether ($C_6H_{13}-O-C_6H_{13}$) species during the SnO_2 NP synthesis reaction, that remain associated with the solid SnO_2 NP samples to the highest temperatures studied here. The spectrum of the sample prepared at 160 °C (Figure 8a) shows a broad signal at 64.9 ppm that can be assigned to the C1 atom of 1-hexanol. This is typically expected to occur at ~62 ppm, and the ~3 ppm increase in chemical shift can be attributed to strong H-bonding interactions with the SnO_2 NP surface. The 6 narrow signals observed at 72.5, 32.3, 30.1, 26.2, 23.1, and 13.3 ppm,

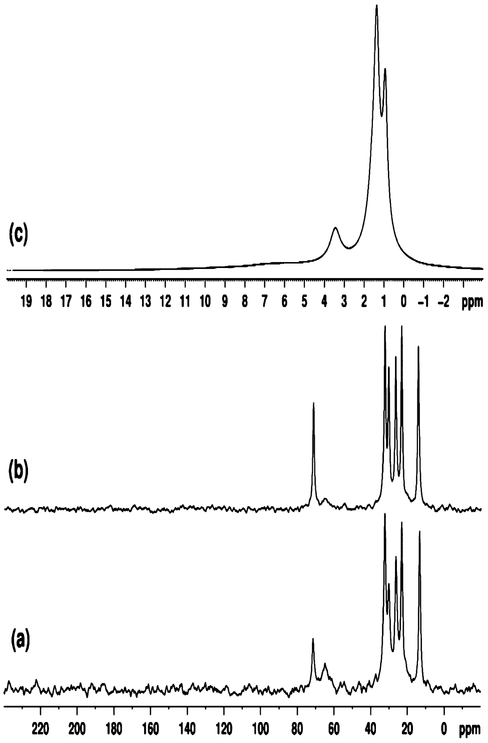

Figure 8. Proton-decoupled ^{13}C MAS (8 kHz) SSNMR spectra of samples prepared at (a) 160 and (b) 200 °C; (c) ^{1}H MAS (12 kHz) NMR spectrum of the sample prepared at 200 °C.

DOI: 10.1021/acsomega.8b02122
ACS Omega 2018, 3, 13227−13238

along with analogous signals at 71.4, 32.5, 30.4, 26.6, 23.3, and 14.3 ppm for the 200 °C sample, can be attributed to the 6 inequivalent carbon environments (C1−C6) of the hexyl (C_6H_{13}−) fragments (Figure 8b). The observed shift at ~72 ppm can suggest dihexyl ether formation due to the change from $-CH_2-O-H$ to $-CH_2-O-CH_2C_5H_{11}$ environments. An additional β-effect of about +10 ppm of the $CH_2C_5H_{11}$ substituent (by analogy with the β-effect of the methyl group)[37−40] acting on the chemical shift of the C1 carbon would be consistent with this assignment. The reported ^{13}C shifts for dihexyl ether in $CDCl_3$ solution at 71.05, 31.85, 29.90, 26.01, 22.71, and 14.02 ppm[37,38] agree with those observed here for samples prepared at 160 and 200 °C. Such high frequency shifts are well known from previous ^{13}C NMR studies. The signals from C2−C6 atoms of dihexyl ether and 1-hexanol are expected to overlap.[37−40] From Figure 8, increasing the synthesis temperature (T_{syn}) from 160 to 200 °C leads to significant decrease of the signal intensity at ~65 ppm, reflecting a decrease in the amount of adsorbed 1-hexanol at higher temperature. From the integral intensities of signals at 72 and 65 ppm, the mole-to-mole ratio of dihexyl ether to 1-hexanol changes from 0.6 at 160 °C to 2.7 at 200 °C. Note that unlike the liquid-state ^{13}C NMR spectrum (Figure 7), no signal was observed at ~45 ppm, indicating the absence of 1-chlorohexane in the ^{13}C MAS SSNMR spectra of the SnO_2 NP samples analyzed (Figure 8).

The ^{1}H MAS spectrum of the sample prepared at 200 °C shows three well-resolved peaks at 3.4, 1.4, and 0.9 ppm (Figure 8c). The signals at 3.4 and 0.9 ppm are assigned to methylene and methyl protons of dihexyl ether. Signals from the remaining methylene protons of dihexyl ether (in positions 2, 3, 4, and 5) overlap, giving rise to the signal with highest intensity at 1.4 ppm. A very broad peak at ~6 ppm can also be observed, that we assign to hydroxyl protons of water and 1-hexanol. The ^{1}H MAS spectrum of the sample prepared at 160 °C was similar to that shown in Figure 8c, with slightly broader lines. The results definitely indicated the presence of dihexyl ether in the sample prepared at 260 °C. However, no 3.4 ppm signal was observed in the ^{1}H MAS spectrum of one sample prepared at 180 °C, that was subsequently annealed at 240 °C.

In order to gain insight into the structural differences between SnO_2 NPs synthesized at different temperatures, ^{119}Sn SSNMR measurements were undertaken using 300 MHz (Figure 9) and 600 MHz NMR instruments. The half-height linewidths of the isotropic peaks in ^{119}Sn MAS NMR spectra measured on a 600 MHz NMR instrument were as follows: 1.2 ± 0.1 kHz (T_{syn} = 180 °C, annealed at 240 °C for 72 h) and 8 ± 0.5 kHz (T_{syn} = 200 °C). Previously, Tunstall et al. measured ^{119}Sn NMR parameters of a series of SnO_2 samples with powder sizes varying between 4 and 32 nm in comparison with data for standard bulk cassiterite SnO_2 powder (~10 μm) using a 500 MHz NMR spectrometer.[41] In their case, the observed linewidths were between 0.6 and 1.7 kHz, which is significantly less than that measured in this work for our sample prepared at 200 °C.

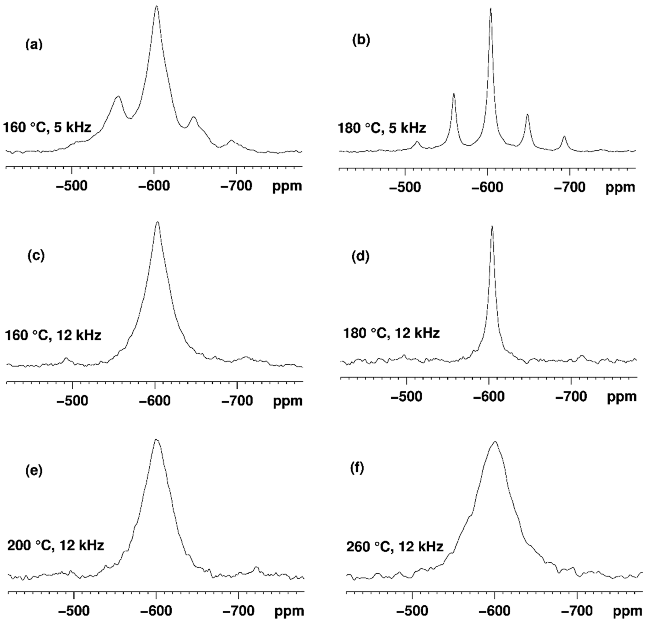

Figure 9. ^{119}Sn MAS SSNMR spectra of SnO_2 samples prepared at (a) 160 °C (MAS 5 kHz); (b) 180 °C (MAS 5 kHz); (c) 160 °C (MAS 12 kHz); (d) 180 °C (MAS 12 kHz); (e) 200 °C (MAS 12 kHz); and (f) 260 °C (MAS 12 kHz). Unlike other samples, the sample prepared at 180 °C was subsequently annealed at 240 °C for 72 h.

We attribute such unusually large signal widths to the small average particle sizes achieved in our studies (<8 nm, where the sample properties are dominated by surface rather than bulk effects),[41] combined with an increase in defect densities noted for the NPs from WPPM and HRTEM analysis. The linewidths of the isotropic peaks in ^{119}Sn MAS NMR spectra measured on a 300 MHz NMR instrument were as follows: 3.5 ± 0.2 kHz (T_{syn} = 160 °C), 0.68 ± 0.05 kHz (T_{syn} = 180 °C, then annealed at 240 °C for 72 h), 4.4 ± 0.2 kHz (T_{syn} = 200 °C), and 5.2 ± 0.5 kHz (T_{syn} = 260 °C). In previous work, the ^{119}Sn NMR linewidths were found to increase with decreasing particle size. However, our results suggest the opposite behavior. This could be partly due to the increase in dislocation densities determined by WPPM analysis of our XRPD data. The observation of broad lines and their field dependence are also similar to those described by Alla and Lippmaa,[42] which they attribute to the anisotropy of the magnetic susceptibility, $\Delta\chi_v$. They showed that adamantane mixed at a 1:10 ratio with *p*-dibromobenzene shows severely broadened ^{13}C lines due to the magnetic field produced by crystallites of *p*-dibromobenzene surrounding the adamantane particles. Similar arguments could apply in the case of SnO_2 NPs, where each ^{119}Sn environment experiences the magnetic field produced by large numbers of smaller SnO_2 NPs, leading to broadened lines. Only the sample prepared at 180 °C and annealed at 240 °C shows narrow lines in the ^{119}Sn NMR spectrum, and this is likely due to sintering of the NPs causing agglomeration into larger crystallites.[41] There is a noticeable line narrowing on proton decoupling, giving rise to the following isotropic linewidths measured on a 300 MHz NMR instrument: 3.2 ± 0.2 kHz (160 °C), 0.67 ± 0.05 kHz (180 °C, annealed at 240 °C for 72 h), 4.1 ± 0.2 kHz (200 °C), and 4.9 ± 0.5 kHz (260 °C). This agrees with the ^{1}H and ^{13}C NMR results that indicate that organic species and water are adsorbed on the surface of the SnO_2 NPs. The close proximity of protons to the tin atoms of SnO_2 leads to additional broadening due to $^{1}H-^{119}Sn$ dipolar interactions in ^{119}Sn MAS spectra without proton decoupling.

We estimated the ^{119}Sn chemical shift anisotropy (CSA, $\Delta\delta$) and the asymmetry parameter (η) for our samples.[43] As a reference, we used values for crystalline SnO_2, although we note that there is some disagreement in previously reported

^{119}Sn CSA parameters for the cassiterite phase. Clayden et al.[44] reported $\Delta\delta/\eta$ values of −125 ppm/0, while Cossement et al.[43] found −125 ppm/0.27. From iterative Herzfeld−Berger analysis of the spinning sideband intensities using the HBA program[43,44] in the ^{119}Sn NMR spectrum recorded at a magic-angle spinning (MAS) frequency of 5 kHz at 7.05 T for the sample prepared at 180 °C, our best-fit $\Delta\delta/\eta$ values are −134 ppm/0.55, with $\delta_{11} = -535$ ppm, $\delta_{22} = -584$ ppm, $\delta_{33} = -693$ ppm, and $\delta_{\text{iso}} = -604$ ppm. These are in agreement with the best-fit $\Delta\delta/\eta$ values of −136 ppm/0.50 ($\delta_{11} = -536$ ppm, $\delta_{22} = -581$ ppm, $\delta_{33} = -695$ ppm, and $\delta_{\text{iso}} = -604$ ppm) determined from analysis of the ^{119}Sn NMR spectrum recorded at a MAS frequency of 10 kHz at 14.1 T for the same sample. Our best-fit CSA parameters determined from the analysis of spinning sideband intensities at a MAS frequency of 5 kHz were $\Delta\delta = -131$ ppm and $\eta = 0.37$ ($\delta_{11} = -542$ ppm, $\delta_{22} = -575$ ppm, $\delta_{33} = -690$ ppm, and $\delta_{\text{iso}} = -603$ ppm) for the 160 °C sample and $\Delta\delta = -134$ ppm and $\eta = 0.50$ ($\delta_{11} = -535$ ppm, $\delta_{22} = -580$ ppm, $\delta_{33} = -691$ ppm, and $\delta_{\text{iso}} = -602$ ppm) for that prepared at 200 °C. Because of the very large linewidths, these can be only considered as approximate estimates, although they demonstrate an increase in values compared to those for bulk cassiterite[43,44] with an average particle size ≈ 10 μm.[41] Such changes in the ^{119}Sn CSA parameters are commensurate with the increased number of Sn sites near the SnO_2 NP surface compared to bulk atoms in nanometer-sized NPs.

2.4. IR and Raman Spectroscopy. Fourier transform infrared (FTIR) spectra of the samples showed strong absorption occurring between 400 and 750 cm^{-1} with two main maxima observed near 650 and 545 cm^{-1} (Figure 10). These features are typical of SnO_2 NPs and are related to asymmetric and symmetric Sn−O stretching vibrations of the bulk phase.[45] The lower wavenumber component is slightly enhanced for samples prepared at lower temperature that have a smaller NP size, whereas an additional structure begins to be observed on the higher frequency band of the 260 °C sample, approaching the IR spectra of bulk SnO_2 powders.[46] The strong asymmetric band with its maximum near 3450 cm^{-1} indicates the presence of adsorbed molecular H_2O on the surface of the NP samples. This also gives rise to the feature near 1630 cm^{-1} due to H−O−H bending. The SnO_2 NPs readily adsorb molecular H_2O from the atmosphere, as demonstrated by our thermogravimetric (TGA) analyses of samples that had been exposed to air (Figure S2).

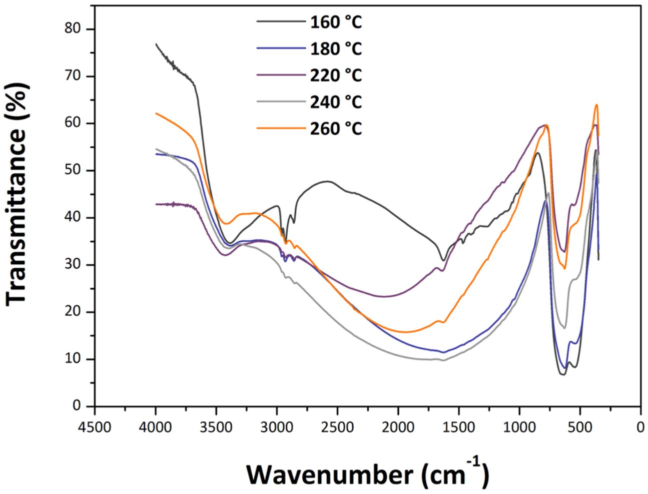

Figure 10. FTIR spectra of the samples containing SnO_2 NPs produced by the reaction between $SnCl_4$ and 1-hexanol at different temperatures.

The aliphatic C−H stretching peaks between 2850 and 2950 cm^{-1} confirm our NMR results that organic species derived from the 1-hexanol reactant remain present within the solid samples. These features are particularly strong for the sample synthesized at 160 °C, but they remain present to the highest synthesis temperatures studied here, suggesting that the organic species remain strongly bound to the external surfaces of the NPs. We do not yet have a good interpretation for the broad absorption feature observed between approximately 1000 and 3000 cm^{-1}, that has a maximum that moves to different wavelengths as a function of synthesis temperature, although it could be related to a light scattering effect associated with the dielectric SnO_2 NPs. Raman spectra were obtained for several series of SnO_2 NPs prepared in this study, using different instruments and excitation wavelengths. Representative data obtained with 514.5 nm laser excitation are shown in Figure 11. The spectra in the 400−700 cm^{-1} range are similar to observations by Diéguez et al.,[47] with broad bands dominated by surface rather than bulk modes (Figure 11b). Bulk crystalline SnO_2 with a tetragonal rutile structure ($P4_2/mnm$ space group) exhibits four Raman active peaks due to zone center vibrations: A_{1g} (634 cm^{-1}), B_{2g} (773 cm^{-1}), E_g (473 cm^{-1}), and a low frequency (123 cm^{-1}) B_{1g} mode that is not reported in all studies. For highly crystalline materials including NPs with sizes above 75−100 nm, the spectra are dominated by the strong A_{1g} mode that becomes broadened and shift to a lower wavenumber as the particle size decreases.[48] The B_{2g} and E_g peaks become less visible, and broad features appear between 450−600 and 750−800 cm^{-1}, corresponding to vibrational excitations in the density of states function ($g(\omega)$) that become activated as the particle size is reduced. In addition, a weak peak due to a normally IR-active A_{2u} LO mode can be observed as a surface mode in larger NPs, while a further surface mode is reported to occur at 543 cm^{-1}.[48] As the NPs develop sizes below ∼15 nm, a broad feature near 572 cm^{-1} begins to dominate the spectrum.[47,49] This mode along with other weak features has also been associated with surface vibrations. Our spectra provide new information on features in the low wavenumber (200−400 cm^{-1}) region, which correspond roughly with the ($g(\omega)$) profile for the bulk crystalline phase.[50] Additional Raman features can also become activated because of the presence of defects, including screw dislocations, as shown by our X-ray WPPM analysis and HRTEM observations.[51] Consistent with Diéguez et al,[47] the A_{1g} mode broadens and shifts to a lower wavenumber as the NP size decreases, while the frequencies of B_{2g} and E_g modes approach that of the A_{1g} vibration. Our samples show broad bands in the 1350−1600 cm^{-1} range and near 3000 cm^{-1} because of the presence of 1-hexanol and dihexyl ether attached to the NP surface as detected by NMR spectroscopy.[47]

2.5. UV−Visible Optical Spectroscopy and Band Gap Determination. UV−visible spectra were obtained for the SnO_2 NP samples using diffuse reflectance spectroscopy (DRS) (Figure 12). The UV−vis data were transformed into an absorbance scale by Kubelka−Munk analysis and optical E_g values determined using the Tauc method (Figure 13). The direct E_g for bulk SnO_2 occurs at 3.60 eV.[51,52] For SnO_2 NPs, there is on-going discussion about the direct versus indirect

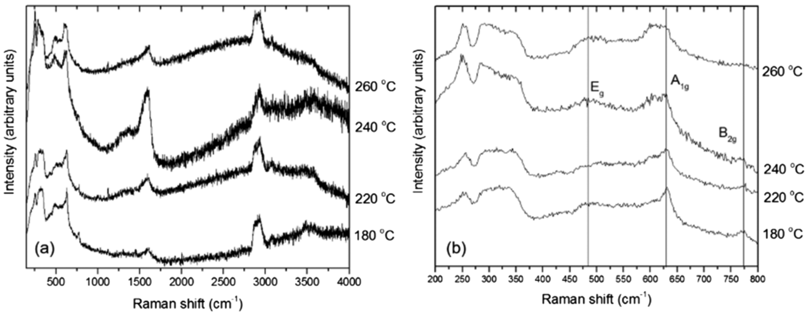

Figure 11. Raman spectra of SnO_2 samples prepared at 180, 220, 240, and 260 °C recorded using 514.5 nm excitation. (a) 200−4000 cm^{-1} wavenumber range; (b) 200−800 cm^{-1} wavenumber range.

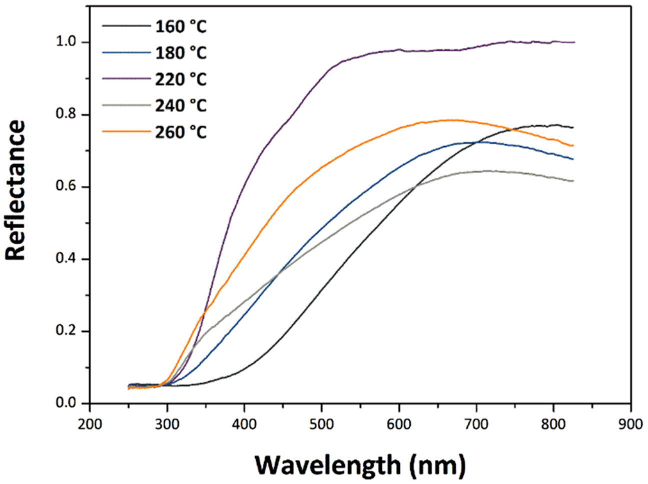

Figure 12. UV−vis diffuse reflectance spectra of SnO_2 NP specimens prepared at different temperatures.

nature of the interband transition.[53−56] For this reason, we examined both $(\alpha h\nu)^2$ and $(\alpha h\nu)^{1/2}$ versus photon energy plots to determine E_g (Figure 13a,b). We note that the direct gap model yields E_g values that are systematically larger than with the indirect gap analysis, and it leads to values that exceed that of bulk SnO_2 for our NPs prepared at the highest temperatures. However, if the transition is indirect, it is found to approach the bulk value for the largest samples (Table 3). In both models, the E_g values increase with NP size and synthesis temperature. This observation contrasts with previous studies that have typically found an increase in the band gap of undoped SnO_2 NPs for smaller particle sizes.[23,24,26,57] Here, we suggest an interpretation of our result based on the observed changes in structural parameters with NP size and preparation temperature, along with the presence of organic ligands derived from the synthesis decorating the NP surface.

Our analyses of the XRPD data show that the NPs all have the same unit cell volume (0.072 nm^3). This is approximately 6−7% smaller than the bulk value (0.7687 nm^3), indicating that our SnO_2 NPs are in a state of lattice compression compared with the bulk material. There is also a slight change in the a_o and c_o lattice parameters, with the smallest NPs prepared at lowest T_{syn} having the smallest c/a ratio (0.6703) rising to 0.6714 for the larger NPs (Table 1). Both values are larger than the value for bulk SnO_2 (0.6680), indicating a systematic increase in the degree of axial strain. Both tensile and compressive strains are known to modify E_g in SnO_2 and other semiconductors, as well as the direct versus indirect nature of the interband transition.[20,58] We suggest that these lattice strains could be linked to the presence of organic ligands derived from the synthesis procedure decorating the growing NP surfaces. The smallest NPs prepared at lowest temperature show the smallest axial strain values and both their direct and indirect E_g values are smaller than the bulk material. We can

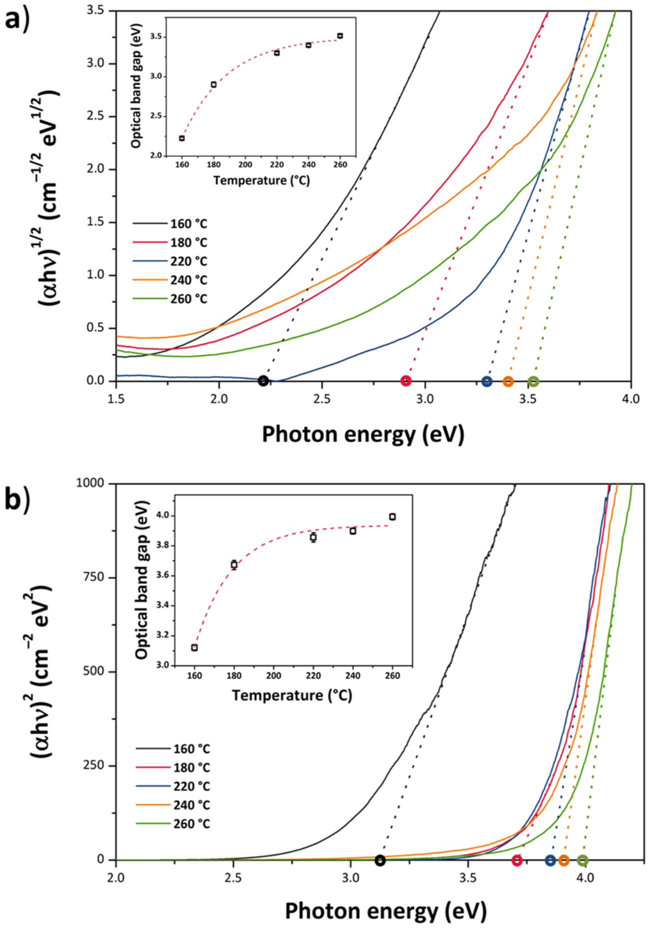

Figure 13. Plots of the Kubelka−Munk function vs photon energy of the specimens synthesized at different temperatures showing the optical E_g estimated using the Tauc procedure. The dashed lines represent the x-axis intercept of the line tangent to the inflection point for each dataset. (a) Indirect E_g model, $[F(R_\infty)h\nu]^{1/2}$, $\gamma = 2$. The insets show the systematic changes in E_g with increasing synthesis temperature and resulting NP size. (b) Directly allowed E_g model—$[F(R_\infty)h\nu]^2$, $\gamma = 1/2$; the red dashed lines are drawn as a guide for the eye, showing an approximately exponential trend for the evolution of the optical E_g with the increase in the synthesis temperature.

Table 3. Optical Band Gap (E_g) of the SnO_2 NP Specimens, as Calculated from the UV−Vis Data Using the Tauc Procedure

	optical E_g (eV)	
synthesis temperature (°C)	direct, $\gamma = 1/2$	indirect, $\gamma = 2$
160	3.12 ± 0.02	2.22 ± 0.02
180	3.67 ± 0.03	2.90 ± 0.03
220	3.86 ± 0.03	3.30 ± 0.02
240	3.90 ± 0.02	3.40 ± 0.02
260	3.99 ± 0.02	3.53 ± 0.02

relate this effect to the overall state of compression of the NPs, along with the c/a ratio that is 0.3% greater than the bulk material. As the NPs grow in size with higher synthesis temperature, we observe an increase in the c/a ratio along with an increased screw dislocation density (Figure 4, Table 1). The band gap shows a regular increase with the axial distortion, while the NPs remain in a similar compressed state, to either approach or exceed the bulk value depending on whether the transition is direct or indirect (Figure 14). The increased concentration of screw dislocations determined by WPPM modeling of the XRPD data testifies to the presence of mechanical strains within the SnO_2 NPs synthesized by our low temperature nonaqueous sol−gel method (cf. Figure 14, top panel).

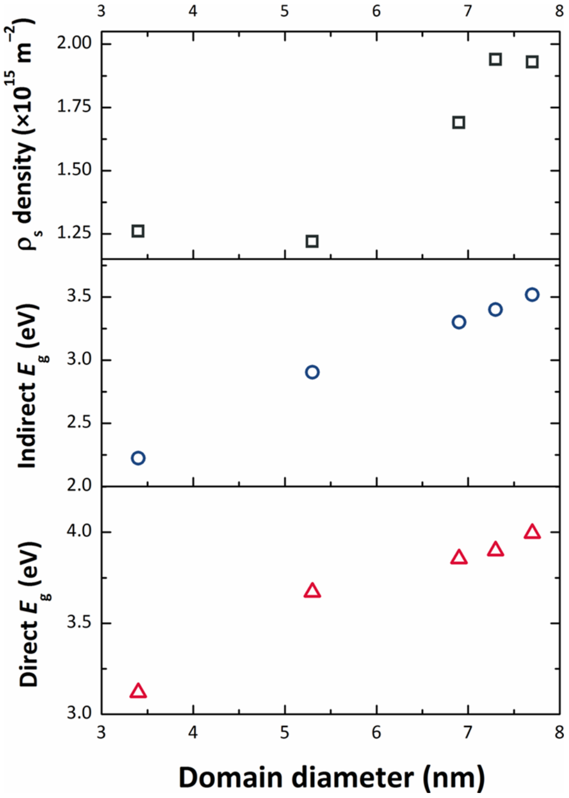

Figure 14. Evolution of the optical gap E_g (bottom panel: direct E_g vs domain diameter; middle panel: indirect E_g vs domain diameter) and the screw dislocation density with the average domain diameter (top panel).

We also note that our UV−visible spectra show significant tailing effects at longer wavelengths, especially for the samples prepared at lowest T. This effect could be partly due to organic ligands attached to the NP surface inducing ligand-to-metal charge transfer transitions[59] (Figure 12). Similar effects were noted by Wang et al. for carbon-coated SnO_2 NPs,[60] where the authors suggested that the outer carbonaceous layer could photosensitize SnO_2, extending the light absorption into the visible range. The absorption tails could also be associated with interband defect states associated with mechanical strains or O^{2-} vacancies within or at the surface of the NPs. We modeled the Urbach energies (E_u) associated with such possible defect states as ∼278 meV.[51]

3. CONCLUSIONS

We have demonstrated a novel low-temperature (160−260 °C) solvothermal route to achieve crystalline SnO_2 NPs using a one-pot nonhydrolytic sol−gel synthesis method. The use of a readily available short chain alcohol (1-hexanol) as the reaction medium and as one of the reagents provides a potentially scalable process, leading to SnO_2 NPs with very small and controllable NP sizes within a narrow dispersion range. The reaction between $SnCl_4$ and 1-hexanol avoids the use of expensive and toxic precursors and thus offers an environmentally benign, inexpensive, and size-selected process for production of SnO_2 NPs with tunable optoelectronic properties. The nonaqueous sol−gel method, together with the WPPM analysis of XRPD data—combined with HRTEM imaging—allowed us to engineer functionally active NPs, determine the NP sizes, and identify screw dislocations present within the SnO_2 NPs in detail. This was further confirmed by HRTEM imaging.

We studied changes in the optical band gap E_g by analysis of UV−visible spectroscopic data. Our results indicated that E_g was smaller than that for bulk SnO_2 for the smallest particles but increased with NP size, contrary to previous findings. If we assumed a direct gap model for interband transitions, our value estimated for >3.5 nm particles exceeded that of the bulk solid, whereas indirect gap analysis showed values approaching the bulk for larger NPs prepared at higher temperature. We suggest that the unexpected variation in E_g with a NP size is due to internal strain parameters developed within the NPs that also lead to an increase in screw dislocation densities observed at higher temperatures, as the particles become larger. The internal strains may be associated with the presence of organic ligands attached to the growing NP surfaces derived from the synthesis reaction. Our simple, low-cost synthetic method leads to new possibilities for tailoring the E_g of SnO_2 nanomaterials as a function of NP size, surface decoration, and the presence or relaxation of internal mechanical strains. Such an approach can allow further tuning of the electronic properties and visible light transparency of SnO_2 NPs for optoelectronic devices.

4. EXPERIMENTAL SECTION

4.1. Synthesis of SnO_2 NPs.

Tin(IV) chloride (99.995%) and anhydrous 1-hexanol (99%) were used as obtained from Aldrich. The syntheses were carried out in a glovebox under controlled environmental conditions (O_2 and H_2O < 1 ppm). In a typical procedure, 1 mmol (0.2603 g) of tin(IV) chloride was added to 20 mL of 1-hexanol, and the mixture was transferred into a stainless-steel autoclave and sealed. The autoclave was taken out of the glovebox and heated in a furnace at between 160 and 260 °C for 3 days. The resulting milky suspensions were centrifuged, and the precipitates were washed with ethanol and dichloromethane and dried in air at 60 °C.

4.2. Sample Characterization. The SnO_2 NPs were studied by XRPD using a θ/θ diffractometer (PANanalytical X'Pert Pro, NL) equipped with a fast RTMS detector, using Cu Kα radiation (45 kV, 40 mA), in the 20−125° 2θ range, with a virtual step scan of 0.1° 2θ, and a virtual time per step of 500 s. The diffraction profiles were analyzed via the WPPM approach,[27−33] using the PM2K software suite.[34] This powerful new technique allows extraction of microstructural information from a powder diffraction pattern, by refining model parameters via a nonlinear least squares fitting routine, fit to the experimental data profile. Within the WPPM method, there is no need for modeling the data using arbitrary peak shape functions (e.g., Gaussian, Lorentzian, and Voigt), as the experimental scattering profile is fit as a convolution of instrumental and sample-related physical effects. In this way, the structural analysis is developed by taking into account physical models of not only the lattice parameters but details of the microstructure and lattice defects including planar and screw dislocations.[27−34] The WPPM method provides an assessment of all aspects of the microstructure including the crystallite domain shape, size, and distribution, with effects due to dislocations modeled through the description of a dislocation contrast factor in terms of a crystallographic invariant.[29,32] It provides considerably more detailed information compared with other integral methods for line profile analysis of XRPD data, such as the routinely used Scherrer formula,[61] or the Williamson−Hall approach.[62] In these methods, instrumental profile components, background and peak profile overlap can play an unwanted role in correctly extracting integral breadths.[61,62] Furthermore, additional sources of line broadening and peak asymmetry, including domain size, lattice strain, and the presence of lattice defects, cannot be investigated in detail.[63] Here, the instrumental contribution to the XRPD profile was calibrated by modeling 14 *hkl* reflections from the NIST SRM 660b standard (LaB_6), according to the Caglioti et al. relationship.[64] Then, SnO_2 described within space group $P4_2/mnm$ for the tetragonal rutile structure was introduced in the WPPM modeling of the data, and the following parameters were refined: background (modeled using a 4th-order shifted Chebyshev polynomial function), peak intensities, specimen displacement, mean and variance of the NP size distributions, and lattice parameters. For simplicity, the crystalline diffracting domains were assumed to be spherical and that their diameter was distributed according to a log-normal size distribution. Both edge and screw dislocations having densities of ρ_e and ρ_s, respectively, were initially assumed to be present in the $10\bar{1}$ {101} slip system, as was shown by Koffyberg [Burgers vector equal to $(a_0^2 + c_0^2)^{1/2}$, with a_0 and c_0 being the lattice parameters],[65] and validated recently by Scardi's group by means of the WPPM method.[33,35] Our HRTEM images (see below) showed that screw dislocations constituted the main defect observed in the NPs, and hence, these were considered to be the only source of anisotropy in the XRPD line profile broadening.

Transmission electron microscopy (TEM) was performed using a Jeol-2000 FXII microscope, with point-to-point and line-to-line resolutions of 0.28 and 0.14 nm, respectively. Additional high-resolution TEM (HRTEM) images were obtained using a JEOL 2200FS microscope with a field-emission gun, operated at 200 kV. Samples for TEM/HRTEM observations were prepared by dispersing the NPs in ethanol and methanol, respectively, and evaporating the suspension drops on carbon-coated Cu grids.

FTIR spectra were obtained using a Bruker Tensor 27 spectrometer. The IR measurements were carried out over the wavenumber range 4000−350 cm^{-1}. Sample powders (2 mg) were mixed with KBr (200 mg, to give ~1 wt % of powder in the KBr disks) and pressed into thin pellets. Raman spectra were measured using a Renishaw micro-Raman instrument with excitation wavelengths of 325 and 514.5 nm. DRS was used to evaluate the optical properties of SnO_2 in the UV−visible range. Spectra were acquired using a Shimadzu UV 3100 (JP) spectrometer equipped with a $BaSO_4$ integrating sphere in the 825−250 nm range, with 0.2 nm in step size, and using $BaSO_4$ as white reference material. The diffuse reflectance data (R_∞) were converted into an absorption coefficient α using the Kubelka−Munk transformation[66]

$$\alpha \approx \frac{k}{S} = \frac{(1 - R_\infty)^2}{2R_\infty} \equiv F(R_\infty)$$

Here, k is the wavelength-dependent absorption coefficient ($k = 4\pi\kappa/\lambda$) and S is a scattering coefficient, assumed to be constant over the wavelength range. The optical band gap E_g of the SnO_2 NPs was assessed by the Tauc procedure that assumes the absorption coefficient α of a semiconductor can be expressed as

$$(\alpha h\nu) = A(h\nu - E_g)^\gamma$$

where A is a material-dependent constant, h is Planck's constant, and ν is the light frequency. The power coefficient γ is characteristic of the type of transition considered, with a value of 1/2 or 2 depending on whether the transition is directly or indirectly allowed.[67] There is still not agreement on whether the band-to-band transition in SnO_2 NPs is direct or indirect.[7,53,54] We tested both solutions to estimate E_g values in our study. We fitted the plots given by the transformed Kubelka−Munk equation $[F(R_\infty)h\nu]^\gamma$ versus $h\nu$ using a sigmoidal Boltzmann function (Origin ProLab, version 8.5.0). The x-axis intercept of the line tangent to the inflection point of the appropriate curve provided direct versus indirect gap model estimates for each of our SnO_2 NP samples.

Liquid-state ^1H and ^{13}C NMR spectroscopies were used to investigate the organic species formed during the reaction and remaining in the supernatant liquid after centrifugation. Spectra were measured in $CDCl_3$ solutions using a 300 MHz Bruker AVANCE NMR spectrometer. Solid-state NMR experiments to study the SnO_2 NPs were carried out at ambient probe temperature on a Bruker AVANCE 300 spectrometer with a 7.05 T wide-bore magnet. High-resolution solid-state ^1H, ^{13}C, and ^{119}Sn NMR spectra were recorded at 300.1, 75.5, and 111.9 MHz, respectively, using a standard Bruker 4 mm double-resonance MAS probe. Powdered solid materials were packed into zirconia rotors of 4 mm external diameter and spun at MAS frequencies of 3−12 kHz with stability better than ±3 Hz. High-resolution solid-state ^{13}C NMR spectra were recorded using MAS, with high-power proton decoupling and the pulse sequence of Cory and Ritchey[68] with the suppression of extraneous signals originating from materials outside the NMR coil. Typical acquisition conditions for ^{13}C NMR experiments were as follows: ^{13}C 90° pulse duration = 3.0 μs; recycle delay = 10 s; number of transients 6000−17 200. Solid-state ^{13}C MAS spectra with high-power proton decoupling and cross-polarization (CP) from protons were also acquired for the sample prepared at 200 °C, with the following acquisition conditions: ^{1}H 90° pulse duration = 4.0 μs; recycle delay = 5 s; and number of transients 3400. However, the ^{13}C CPMAS spectrum showed a poorer signal-to-noise ratio compared to that acquired using the sequence of Cory and Ritchey[69] with the direct detection of ^{13}C nuclei. Solid-state ^{119}Sn MAS spectra at 111.9 MHz with and without high-power proton decoupling were recorded using the following acquisition conditions: ^{119}Sn 60° pulse duration = 1.5 μs; recycle delay = 10−30 s; number of transients 2000−30 000, and MAS frequency = 3−12 kHz. Additionally, ^{119}Sn SSNMR spectra were recorded on a Bruker AVANCE 600 MHz spectrometer at the resonance frequency of 223.8 MHz using the following acquisition conditions: ^{119}Sn 45° pulse duration = 2.0 μs; recycle delay = 5 s; number of transients 1500−12 300, and MAS frequency = 10−12 kHz. The sequence used to collect ^{1}H MAS NMR spectra at 300.1 MHz comprised a single-pulse excitation with a 2.4 μs long pulse (recycle delay = 5 s; number of transients 8−32, and MAS frequency = 8−12 kHz). The ^{13}C and ^{1}H chemical shifts are given relative to tetramethylsilane (TMS), which were calibrated using glycine (176.46 ppm) and tetrakis(trimethylstannyl)methane doped with TMS (0 ppm), respectively. The ^{119}Sn chemical shifts are given relative to tetramethyltin $SnMe_4$, calibrated using tetrakis(trimethylstannyl)methane $C(SnMe_3)_4$ (48.2 ppm).[69] In the case of the ^{119}Sn CSA ($\Delta\delta$) for SnO_2 with $\delta < 0$, parameters are defined as follows

$$\text{Principal CSA components } \delta_{11} \geq \delta_{22} \geq \delta_{33}$$

$$\text{Isotropic value } \delta_{\text{iso}} = (\delta_{11} + \delta_{22} + \delta_{33})/3$$

$$\text{Chemical shift anisotropy } \Delta\delta = \delta_{33} - (\delta_{11} + \delta_{22})/2$$

$$\text{Asymmetry parameter } \eta = (\delta_{22} - \delta_{11})/(\delta_{33} - \delta_{\text{iso}}) \text{ with } 0 \leq \eta \leq 1$$

Here, the principal components of the chemical shift tensor, δ_{11}, δ_{22}, and δ_{33}, are defined such that the highest frequency (the least shielded) component is labeled as δ_{11}, while δ_{33} corresponds to the lowest frequency (the most shielded) component.

ASSOCIATED CONTENT

Supporting Information

The Supporting Information is available free of charge on the ACS Publications website at DOI: 10.1021/acsomega.8b02122.

> ^{1}H NMR spectrum of the filtered reaction solution measured in $CDCl_3$ of the SnO_2 NPs; TGA of the SnO_2 NP samples synthesized at different temperatures; and ^{13}C NMR chemical shift values for key organic species discussed in the text (PDF)

AUTHOR INFORMATION

Corresponding Authors

*E-mail: karmaoui@ua.pt, karmaoui.mohamed@univ-usto.dz, m.karmaoui@surrey.ac.uk (M.K.).
*E-mail: david.tobaldi@ua.pt, david@davidtobaldi.org (D.M.T.).

ORCID

Mohamed Karmaoui: 0000-0002-2288-6290
Paul F. McMillan: 0000-0002-5298-780X
Robert C. Pullar: 0000-0001-6844-4482
David Maria Tobaldi: 0000-0002-0112-8570

Notes

The authors declare no competing financial interest.

ACKNOWLEDGMENTS

M.K. thanks Fundação para a Ciência e a Tecnologia (FCT) for grant no. SFRH/BPD/74477/2010. This work was developed within the scope of the project CICECO−Aveiro Institute of Materials, POCI-01-0145-FEDER-007679 (FCT Ref. UID/CTM/50011/2013), financed by national funds through the FCT/MEC and when appropriate co-financed by FEDER under the PT2020 Partnership Agreement. R.C.P. thanks FCT grant IF/00681/2015 for supporting this work. Dr Harold Toms is thanked for assistance performing SSNMR measurements.

DEDICATION

We dedicate this work to the memory of our colleague and friend, Dr Russell Binions, who passed away unexpectedly during the preparation of this manuscript.

REFERENCES

(1) Das, S.; Jayaraman, V. SnO_2: A comprehensive review on structures and gas sensors. *Prog. Mater. Sci.* **2014**, *66*, 112−255.

(2) Chen, Z.; Pan, D.; Li, Z.; Jiao, Z.; Wu, M.; Shek, C.-H.; Wu, C. M. L.; Lai, J. K. L. Recent Advances in Tin Dioxide Materials: Some Developments in Thin Films, Nanowires, and Nanorods. *Chem. Rev.* **2014**, *114*, 7442−7486.

(3) Kamat, P. V. Dominance of Metal Oxides in the Era of Nanotechnology. *J. Phys. Chem. Lett.* **2011**, *2*, 839−840.

(4) Wang, J.; Lian, G.; Si, H.; Wang, Q.; Cui, D.; Wong, C.-P. Pressure-Induced Oriented Attachment Growth of Large-Size Crystals for Constructing 3D Ordered Superstructures. *ACS Nano* **2016**, *10*, 405−412.

(5) Ma, N.; Suematsu, K.; Yuasa, M.; Kida, T.; Shimanoe, K. Effect of Water Vapor on Pd-Loaded SnO_2 Nanoparticles Gas Sensor. *ACS Appl. Mater. Interfaces* **2015**, *7*, 5863−5869.

(6) Bae, J.-Y.; Park, J.; Kim, H. Y.; Kim, H.-S.; Park, J.-S. Facile Route to the Controlled Synthesis of Tetragonal and Orthorhombic SnO_2 Films by Mist Chemical Vapor Deposition. *ACS Appl. Mater. Interfaces* **2015**, *7*, 12074−12079.

(7) Xu, X.; Zhuang, J.; Wang, X. SnO_2 Quantum Dots and Quantum Wires: Controllable Synthesis, Self-Assembled 2D Architectures, and Gas-Sensing Properties. *J. Am. Chem. Soc.* **2008**, *130*, 12527−12535.

(8) Zhu, Y.; Guo, H.; Zhai, H.; Cao, C. Microwave-Assisted and Gram-Scale Synthesis of Ultrathin SnO_2 Nanosheets with Enhanced Lithium Storage Properties. *ACS Appl. Mater. Interfaces* **2015**, *7*, 2745−2753.

(9) Lavanya, N.; Radhakrishnan, S.; Sudhan, N.; Sekar, C.; Leonardi, S. G.; Cannilla, C.; Neri, G. Fabrication of folic acid sensor based on the Cu doped SnO_2 nanoparticles modified glassy carbon electrode. *Nanotechnology* **2014**, *25*, 295501.

(10) Sarmah, S.; Kumar, A. Optical properties of SnO_2 nanoparticles. *Indian J. Phys.* **2010**, *84*, 1211−1221.

(11) Chiu, H.-C.; Yeh, C.-S. Hydrothermal Synthesis of SnO_2 Nanoparticles and Their Gas-Sensing of Alcohol. *J. Phys. Chem. C* **2007**, *111*, 7256−7259.

(12) Wang, X.; Wang, Y.; Tian, F.; Liang, H.; Wang, K.; Zhao, X.; Lu, Z.; Jiang, K.; Yang, L.; Lou, X. From the Surface Reaction Control to Gas-Diffusion Control: The Synthesis of Hierarchical Porous SnO_2

Microspheres and Their Gas-Sensing Mechanism. *J. Phys. Chem. C* **2015**, *119*, 15963−15976.

(13) Ding, L.; He, S.; Miao, S.; Jorgensen, M. R.; Leubner, S.; Yan, C.; Hickey, S. G.; Eychmüller, A.; Xu, J.; Schmidt, O. G. Ultrasmall SnO_2 Nanocrystals: Hot-bubbling Synthesis, Encapsulation in Carbon Layers and Applications in High Capacity Li-Ion Storage. *Sci. Rep.* **2014**, *4*, 4647.

(14) Karmaoui, M.; Ramana, E. V.; Tobaldi, D. M.; Lajaunie, L.; Graça, M. P.; Arenal, R.; Seabra, M. P.; Labrincha, J. A.; Pullar, R. C. High dielectric constant and capacitance in ultrasmall (2.5 nm) $SrHfO_3$ perovskite nanoparticles produced in a low temperature non-aqueous sol-gel route. *RSC Adv.* **2016**, *6*, 51493−51502.

(15) Karmaoui, M.; Leonardi, S. G.; Latino, M.; Tobaldi, D. M.; Donato, N.; Pullar, R. C.; Seabra, M. P.; Labrincha, J. A.; Neri, G. Pt-decorated In_2O_3 nanoparticles and their ability as a highly sensitive (<10 ppb) acetone sensor for biomedical applications. *Sens. Actuators, B* **2016**, *230*, 697−705.

(16) Karmaoui, M.; Amaral, J. S.; Lajaunie, L.; Puliyalil, H.; Tobaldi, D. M.; Pullar, R. C.; Labrincha, J. A.; Arenal, R.; Cvelbar, U. Smallest Bimetallic $CoPt_3$ Superparamagnetic Nanoparticles. *J. Phys. Chem. Lett.* **2016**, *7*, 4039−4046.

(17) Karmaoui, M.; Lajaunie, L.; Tobaldi, D. M.; Leonardi, G.; Benbayer, C.; Arenal, R.; Labrincha, J. A.; Neri, G. Modification of anatase using noble-metals (Au, Pt, Ag): Toward a nanoheterojunction exhibiting simultaneously photocatalytic activity and plasmonic gas sensing. *Appl. Catal., B* **2017**, *218*, 370−384.

(18) Pinna, N.; Neri, G.; Antonietti, M.; Niederberger, M. Nonaqueous Synthesis of Nanocrystalline Semiconducting Metal Oxides for Gas Sensing. *Angew. Chem., Int. Ed.* **2004**, *43*, 4345−4349.

(19) Sanon, G.; Rup, R.; Mansingh, A. Band-gap narrowing and band structure in degenerate tin oxide (SnO_2) films. *Phys. Rev. B: Condens. Matter Mater. Phys.* **1991**, *44*, 5672−5680.

(20) Zhou, W.; Liu, Y.; Yang, Y.; Wu, P. Band Gap Engineering of SnO_2 by Epitaxial Strain: Experimental and Theoretical Investigations. *J. Phys. Chem. C* **2014**, *118*, 6448−6453.

(21) Chetri, P.; Choudhury, A. Investigation of optical properties of SnO_2 nanoparticles. *Phys. E* **2013**, *47*, 257−263.

(22) Mendes, P. G.; Moreira, M. L.; Tebcherani, S. M.; Orlandi, M. O.; Andrés, J.; Li, M. S.; Diaz-Mora, N.; Varela, J. A.; Longo, E. SnO_2 nanocrystals synthesized by microwave-assisted hydrothermal method: towards a relationship between structural and optical properties. *J. Nanopart. Res.* **2012**, *14*, 750.

(23) Viter, R.; Katoch, A.; Kim, S. S. Grain size dependent bandgap shift of SnO_2 nanofibers. *Met. Mater. Int.* **2014**, *20*, 163−167.

(24) Sharma, V. An insight into the structural, electrical and optical properties of SnO_2 nanoparticles. *J. Sol-Gel Sci. Technol.* **2017**, *84*, 231−238.

(25) Ahmed, A. S.; Azam, A.; Shafeeq, M. M.; Chaman, M.; Tabassum, S. Temperature dependent structural and optical properties of tin oxide nanoparticles. *J. Phys. Chem. Solids* **2012**, *73*, 943−947.

(26) Pang, G.; Chen, S.; Koltypin, Y.; Zaban, A.; Feng, S.; Gedanken, A. Controlling the Particle Size of Calcined SnO_2 Nanocrystals. *Nano Lett.* **2001**, *1*, 723−726.

(27) Scardi, P.; Leoni, M. Whole powder pattern modelling. *Acta Crystallogr., Sect. A: Found. Crystallogr.* **2002**, *58*, 190−200.

(28) Leoni, M.; Confente, T.; Scardi, P. PM2K: a flexible program implementing Whole Powder Pattern Modelling. *Z. Kristallogr. Suppl.* **2006**, *2006*, 249−254.

(29) Scardi, P.; Leoni, M. Whole Powder Pattern Modelling: Theory and Applications. In *Diffraction Analysis of the Microstructure of Materials*; Mittemeijer, I. E. J., Scardi, P., Eds.; Springer: Berlin, 2004; pp 51−91.

(30) Scardi, P.; Leoni, M. Line Profile Analysis: Pattern Modelling versus Profile Fitting. *J. Appl. Crystallogr.* **2006**, *39*, 24−31.

(31) Scardi, P. Microstructural Properties: Lattice Defects and Domain Size Effects. In *Powder Diffraction: Theory and Practice*; Dinnebier, R. E., Billinge, S. J. L., Eds.; RSCPublishing: Cambridge, 2008; pp 376−413.

(32) Scardi, P.; Leoni, M. Diffraction line profiles from polydisperse crystalline systems. *Acta Crystallogr., Sect. A: Found. Crystallogr.* **2001**, *57*, 604−613.

(33) Leoni, M.; Martinez-Garcia, J.; Scardi, P. Dislocation effects in powder diffraction. *J. Appl. Crystallogr.* **2007**, *40*, 719−724.

(34) Leoni, M.; Confente, T.; Scardi, P. PM2K: a flexible program implementing Whole Powder Pattern Modelling. *Z. Kristallogr. Suppl.* **2006**, *2006*, 249−254.

(35) Scardi, P. Recent advancements in Whole Powder Pattern Modelling. *Z. Kristallogr. Suppl.* **2008**, *2008*, 101−111.

(36) Dodoo-Arhin, D.; Nuamah, R. A.; Jain, P. K.; Obada, D. O.; Yaya, A. Nanostructured stannic oxide: Synthesis and characterisation for potential energy storage applications. *Results Phys.* **2018**, *9*, 1391−1402.

(37) Aliev, A. E.; Harris, K. D. M. Probing Hydrogen Bonding in Solids Using Solid State NMR Spectroscopy. In *Supramolecular Assembly via Hydrogen Bonds I*; Mingos, D. M. P., Ed.; Springer Berlin Heidelberg: Berlin, Heidelberg, 2004; pp 1−53.

(38) Wehrli, F. W.; Marchand, A. P.; Wehrli, S. *Interpretation of Carbon-13 NMR Spectra*; Wiley: New York, Brisbane, Toronto, Singapore, 1988.

(39) Breitmaier, E.; Voelter, W. *Carbon-13 NMR Spectroscopy-High Resolution Methods and Applications in Organic Chemistry and Biochemistry*, 3rd ed.; Wiley-VCH, 1986.

(40) Aliev, A. E.; Harris, K. D. M. Conformational properties of monosubstituted cyclohexanes in their thiourea inclusion compounds and in solution: variable-temperature one-dimensional and two-dimensional carbon-13 NMR investigations. *J. Am. Chem. Soc.* **1993**, *115*, 6369−6377.

(41) Tunstall, D. P.; Patou, S.; Liu, R. S.; Kao, Y. H. Size effects in the NMR of SnO_2 powders. *Mater. Res. Bull.* **1999**, *34*, 1513−1520.

(42) Alla, M.; Lippmaa, E. Resolution limits in magic-angle rotation NMR spectra of polycrystalline solids. *Chem. Phys. Lett.* **1982**, *87*, 30−33.

(43) Cossement, C.; Darville, J.; Gilles, J.-M.; Nagy, J. B.; Fernandez, C.; Amoureux, J.-P. Chemical shift anisotropy and indirect coupling in SnO_2 and SnO. *Magn. Reson. Chem.* **1992**, *30*, 263−270.

(44) Clayden, N. J.; Dobson, C. M.; Fern, A. High-resolution solid-state tin-119 nuclear magnetic resonance spectroscopy of ternary tin oxides. *J. Chem. Soc., Dalton Trans.* **1989**, 843−847.

(45) Ayeshamariam, A.; Ramalingam, S.; Bououdina, M.; Jayachandran, M. Preparation and characterizations of SnO_2 nanopowder and spectroscopic (FT-IR, FT-Raman, UV−Visible and NMR) analysis using HF and DFT calculations. *Spectrochim. Acta, Part A* **2014**, *118*, 1135−1143.

(46) Amalric-Popescu, D.; Bozon-Verduraz, F. Infrared studies on SnO_2 and Pd/SnO_2. *Catal. Today* **2001**, *70*, 139−154.

(47) Diéguez, A.; Romano-Rodríguez, A.; Vilà, A.; Morante, J. R. The complete Raman spectrum of nanometric SnO_2 particles. *J. Appl. Phys.* **2001**, *90*, 1550−1557.

(48) Sangeetha, P.; Sasirekha, V.; Ramakrishnan, V. Micro-Raman investigation of tin dioxide nanostructured material based on annealing effect. *J. Raman Spectrosc.* **2011**, *42*, 1634−1639.

(49) Zuo, J.; Xu, C.; Liu, X.; Wang, C.; Hu, Y.; Qian, Y. Study of the Raman spectrum of nanometer SnO_2. *J. Appl. Phys.* **1994**, *75*, 1835−1836.

(50) Gupta, S. D.; Gupta, S. K.; Jha, P. K.; Ovsyuk, N. N. A first principles lattice dynamics and Raman spectra of the ferroelastic rutile to $CaCl_2$ phase transition in SnO_2 at high pressure. *J. Raman Spectrosc.* **2013**, *44*, 926−933.

(51) Porte, Y.; Maller, R.; Faber, H.; AlShareef, H. N.; Anthopoulos, T. D.; McLachlan, M. A. Exploring and controlling intrinsic defect formation in SnO_2 thin films. *J. Mater. Chem. C* **2016**, *4*, 758−765.

(52) Ganose, A. M.; Scanlon, D. O. Band gap and work function tailoring of SnO_2 for improved transparent conducting ability in photovoltaics. *J. Mater. Chem. C* **2016**, *4*, 1467−1475.

(53) Lu, J. G.; Chang, P.; Fan, Z. Quasi-one-dimensional metal oxide materials—Synthesis, properties and applications. *Mater. Sci. Eng., R* **2006**, *52*, 49−91.

(54) Caglar, Y.; Caglar, M.; Ilican, S.; Yakuphanoglu, F. Determination of the electronic parameters of nanostructure SnO_2/p-Si diode. *Microelectron. Eng.* **2009**, *86*, 2072−2077.

(55) Abass, A. K.; Al-Liabi, N. A.; Taha, W. A. Optical properties of bromine-doped SnO_2 coatings for solar applications. *Phys. Status Solidi A* **1988**, *106*, 613−618.

(56) Ginley, D. S. *Handbook of Transparent Conductors*; Springer: Boston, MA, 2010.

(57) Wu, N.-L.; Wang, S.-Y.; Rusakova, I. A. Inhibition of Crystallite Growth in the Sol-Gel Synthesis of Nanocrystalline Metal Oxides. *Science* **1999**, *285*, 1375−1377.

(58) Tsunekawa, S.; Kang, J.; Asami, K.; Kasuya, A. Blueshifts in the ultraviolet absorption spectra of amphoteric SnO_{2-x} nanocrystalline particles. *J. Appl. Phys.* **2002**, *91*, 10098−10102.

(59) Zhang, G.; Kim, G.; Choi, W. Visible light driven photocatalysis mediated via ligand-to-metal charge transfer (LMCT): an alternative approach to solar activation of titania. *Energy Environ. Sci.* **2014**, *7*, 954−966.

(60) Wang, X.; Fan, H.; Ren, P.; Li, M. Carbon coated SnO_2: synthesis, characterization, and photocatalytic performance. *RSC Adv.* **2014**, *4*, 10284−10289.

(61) Klug, H. P.; Alexander, L. E. *X-ray Diffraction Procedures: For Polycrystalline and Amorphous Materials*, 2nd ed.; Wiley, 1974; Vol. *1*, p 992.

(62) Williamson, G. K.; Hall, W. H. X-ray line broadening from filed aluminium and wolfram. *Acta Metall.* **1953**, *1*, 22−31.

(63) Scardi, P.; Leoni, M. Diffraction whole-pattern modelling study of anti-phase domains in Cu_3Au. *Acta Mater.* **2005**, *53*, 5229−5239.

(64) Caglioti, G.; Paoletti, A.; Ricci, F. P. On resolution and luminosity of a neutron diffraction spectrometer for single crystal analysis. *Nucl. Instrum. Methods* **1960**, *9*, 195−198.

(65) Koffyberg, F. P. Etch Pits and Dislocations in SnO_2 Crystals. *J. Appl. Phys.* **1965**, *36*, 844−849.

(66) Marfunin, A. S. *Physics of Minerals and Inorganic Materials: An Introduction*; Springer, 1979.

(67) Wooten, F. Plasmons And Characteristic Energy Losses. *Optical Properties of Solids*; Academic Press, 1972; Chapter 9, pp 210−224.

(68) Cory, D. G.; Ritchey, W. M. Suppression of signals from the probe in bloch decay spectra. *J. Magn. Reson.* **1988**, *80*, 128−132.

(69) Harris, R. K.; Mitchell, T. N.; Nesbitt, G. J. Solid-state tin-119 NMR spectroscopy: The first observations of (Tin-119, tin-117) coupling constants. *Magn. Reson. Chem.* **1985**, *23*, 1080−1081.

DOI: 10.1021/acsomega.8b02122
ACS Omega 2018, 3, 13227−13238